Supporting Information

In-Plane Graphene Moieties Embedded in Carbon Nitride Extend Conjugation, Narrow the Electronic Bandgap and Generate a 10-Fold Enhancement in Visible Light-Driven Photoelectrochemical Performance

Kazi M. Alam,[1] Md Masud Rana,[1] Navneet Kumar,[1] Damini Vrushabendrakumar,[1] Pawan Kumar,[2] Narendra Chaulagain,[1] Harshitha Rajashekhar,[1] John C. Garcia,[1] Guy M. Bernard,[3] Md Golam Kibria,[2] Sergey Gusarov,[4] Vladimir K. Michaelis,[3] Alkiviathes Meldrum,[5] and Karthik Shankar[1]*

[1] Department of Electrical and Computer Engineering, University of Alberta, Edmonton, AB T6G 1H9, Canada

[2] Department of Chemical and Petroleum Engineering, University of Calgary, Calgary, Alberta T2N 1N4, Canada

[3] Department of Chemistry, University of Alberta, Edmonton, Alberta T6G 2G2, Canada

[4] Nanotechnology Research Centre, National Research Council Canada, 11421 Saskatchewan Drive, Edmonton, AB T6G 2M9, Canada

[5] Department of Physics, University of Alberta, Edmonton, Alberta T6G 2E1, Canada

*corresponding authors' email addresses: kshankar@ualberta.ca

* Tel: 780-492-1354; email: kshankar@ualberta.ca

S1. Material Characterizations

CHN combustion analysis: An organic elemental analyzer CHNS/O (Flash 2000, Thermo) equipped with a TCD detector was employed for the CHN combustion analysis. The detection limit of this tool is < 100 ppm.

Field emission scanning electron microscopy (FESEM) imaging and energy dispersive X-ray spectroscopy (EDX) elemental analysis. The morphological features and elemental analysis were characterized using a field emission scanning electron microscope (Zeiss Sigma FESEM) that integrates Oxford Aztec synergy system with EDX. The accelerating voltages for imaging and elemental data collection were 3 kV and 15 kV respectively.

Transmission electron microscopy (TEM) imaging and energy dispersive X-ray spectroscopy (EDX) elemental mapping. JEOL 2200 FS transmission electron microscope (TEM), equipped with a field emission gun was employed for analysing the fine structural features and elemental mapping. The accelerating voltage was kept as 200 kV. Scanning TEM (STEM) mode was used with a nominal probe size of 1 nm for elemental mapping. The high-resolution TEM (HRTEM) image files in. *dm3* format were processed with the Digital Micrograph, Gatan Inc. software.

X-ray absorption near edge structure spectroscopy (XANES). In order to reveal the local chemical structure and coordination pattern of the samples, synchrotron-based X-ray absorption spectroscopy using soft X-rays was employed. X-ray absorption near edge structure (XANES) analysis was performed at the Canadian Light Source (CLS) synchrotron's spherical grating monochromator (SGM) beamline (CLS port 11ID-1) operating in the energy range of 250 to 2000 eV. The room temperature measurements were performed in an ultrahigh vacuum (~10^{-6} Torr) condition. The samples were mounted on a sample holder

using double-sided carbon tape in a vacuum chamber and held at 45° with respect to beam and the detector. Following the completion of evacuation, the samples were irradiated with a soft X-ray where the spot size was kept between 50-100 μm using the Kirkpatrick-Baez mirror system. An Amptek silicon drift detectors (SDDs) with an energy resolution of ~100 eV was used to measure the counts and energy of photons emitted in the process of core hole filling. Both the partial fluorescence and the total electron yields were being measured, so was the SDD detector's signal in order to determine the appropriate location. The final C K-edge and N K-edge spectra were acquired following the averaging of ten consecutive measurements. The SGM beamline laboratory acquisitions and analysis system was used for the data processing and averaging of the XANES signals.

Solid-state nuclear magnetic resonance spectroscopy (NMR). Solid state nuclear magnetic resonance spectroscopy (NMR) was used to elucidate on the local environment of the samples. ^{13}C NMR spectra of solid magic angle spinning samples were obtained on an Avance NEO 300 NMR spectrometer, operating at 75.5 MHz for ^{13}C. Samples were packed into 4 mm outside diameter rotors and spun at 14 kHz. ^{13}C NMR spectra were acquired with single-pulse excitation (SPE), with 62.5 kHz ^{1}H decoupling. For these spectra, the ^{13}C 90° pulse was 4.0 μs, the acquisition time was 38 ms and the recycle delay was 100 s; 588 to 1496 transients were co-added. ^{13}C spectra acquired with SPE are subject to a significant background ^{13}C signal, attributed primarily to the Kel-F rotor caps; to correct for this, a spectrum of an empty rotor was acquired under identical conditions, and its signal was subtracted from those for the samples. Natural abundance ^{15}N NMR spectra of these samples were also acquired on this instrument with the cross polarization (CP) technique. ^{15}N NMR spectra of these samples, spinning at 8 kHz and packed as described above, were acquired on the Avance NEO 300 NMR spectrometer, operating at 30.4 MHz for ^{15}N. The ^{1}H 90° pulse was 4.0 μs, the contact time was 5.0 ms, the acquisition time as 41 ms, and the recycle delay was 5.0 to 10.0 s. These spectra were acquired with 62.5 kHz ^{1}H decoupling. The number of co-added

transients ranged from 42000 to 80000. Note that, because of the inherent insensitivity of natural abundance ^{15}N NMR spectroscopy, acquiring ^{15}N NMR spectra with SPE was impractical and we opted for CP technique instead.

Electron energy loss spectroscopy (EELS). Electron energy-loss spectroscopy (EELS) was employed in order to extract the inner shell ionization edge (core loss) spectra. EELS experiments were conducted on a Hitachi H9500 transmission electron microscope (TEM), equipped with a Lab6 emission gun. The accelerating voltage was 300 kV. The EELS spectra were recorded under the TEM imaging mode on a Gatan GIF Tridium spectrometer. The EELS files in. *dm3* format were processed including the subtraction of background with the Digital Micrograph, Gatan Inc. software.

X-ray photoelectron spectroscopy (XPS) and ultraviolet photoelectron spectroscopy (UPS). The surface chemical composition of the samples and the oxidation states of various constituent elements present in the materials were determined with X-ray photoelectron spectroscopy (XPS) using Axis-Ultra, Kratos Analytical instrument equipped with monochromatic Al-Kα source (15 kV, 50 W) and photon energy of 1486.7 eV under ultrahigh vacuum ($\sim 10^{-8}$ Torr). The binding energy of C1s core level (BE ≈ 284.8 eV) of adventitious hydrocarbon was used for calibration, from which the binding energy of all elements were calculated. XPS was also used to obtain the valence band (VB) spectra of the samples. Ultraviolet photoelectron spectroscopy (UPS) was used to determine the work function (WF) of the samples. A He lamp (21.21 eV) was used as an excitation source. The obtained XPS and UPS raw data were processed in CasaXPS and later plotted in origin software.

Fourier-transform infrared spectroscopy (FTIR). Fourier transform infrared spectroscopy (FTIR) was employed to investigate the chemical bonds and specific functional groups of the material. All spectra

were recorded on a Thermo Nicolet iS50 FTIR spectrometer equipped with a ZnSe based built-in ATR module.

Ultraviolet−visible spectroscopy (UV−Vis). The optical absorption spectra were collected under diffuse reflectance spectroscopy (DRS) mode. A Hitachi U-3900H UV/VIS spectrophotometer equipped with an integrating sphere was used to for this purpose.

Raman spectroscopy. A Raman spectrometer (Renishaw inVia confocal Raman microscope) was used for the Raman spectroscopic analysis in order to extract the vibrational properties of the samples. The excitation wavelength of the Raman laser was 532nm. The incident power was 2 mW, while grating contained 1200 lines mm^{-1}.

Photoluminescence spectroscopy (PL). Steady state photoluminescence spectra of samples were collected on a Varian Cary Eclipse fluorimeter that uses a xenon lamp as the excitation source. The slit width was kept 5 nm for all the samples.

Time resolved photoluminescence spectroscopy (TRPL). Time-resolved photoluminescence (TRPL) spectroscopy was used to study the carrier dynamics. The samples were excited with a 405 nm PICOPOWER LD-405H laser (Alphalas, GmbH) having a nominally 25 ps pulses. An optical filter interfaced through a 425 nm long-pass filter to an intensity calibrated USB-2000 + Ocean Optics miniature spectrometer was primarily used to acquire the photoluminescence spectra. Next, the fiber was disconnected from the spectrometer and directed to an HPM100-50 hybrid single-photon detector. The detector was interfaced to an SPC130-EMN single photon counter and data were collected using the SPCM software package. The detector, single photon counter and software package, all are from Becker-Hickl.

X-ray diffractometry (XRD). X-ray powder diffraction spectra of the samples were collected in order to study the crystalline structure. Data were acquired on a Rigaku Ultima IV XRD, with the radiation source of a Cu X-ray tube (Cu-Kα, $I_{\mu}S_{\mu}$, λ = 0.15418 nm) operating at 40 kV and 44 mA, equipped with a scintillation counter plus graphitic crystal monochromator detector. Experiments were conducted at room temperature with a scan speed of 2°/min.

N_2 adsorption-desorption isotherm. The surface areas of the samples were determined by applying the BET (Brunauer–Emmett–Teller) method to the obtained N_2 adsorption-desorption isotherms. An Autosorb iQ (Quantachrome Instruments) was used to get the N_2 adsorption-desorption isotherm recorded at -190 °C. The samples were outgassed under vacuum at 150 °C for 2 hours first in order to remove all moisture and adsorbed gases on the surface.

Current density-voltage (J-V) measurements. Steady-state current density-voltage (*J-V*) characteristics were obtained using a Keithley 4200A Semiconductor Characterization System (SCS Parameter Analyzer). Measurements were performed in the dark condition.

Photovoltage (PV) and transient photovoltage (TPV) measurements. Photovoltage (PV) and transient photovoltage (TPV) measurements were performed on a Fluxim Paios Spectrometer system, equipped with a white light emitting diode (LED). Variable light intensity was used for a pulse duration of 90 ms prior to the monitoring of the photovoltage decay. The pulse settling time was 10 ms.

S2. ABPE calculation

The applied bias photon-to-current efficiency (ABPE%) was calculated by using the following expression, where the applied voltage is on the RHE (reversible hydrogen electrode) scale.

$$ABPE\ (\%) = J\ (mA\ cm^{-2}\ ) \times \frac{1.23 - V_b}{P(mW\ cm^{-2})} \times 100$$

Where, *J* is the photocurrent density, V_b is the applied voltage at RHE scale and *P* is the power density of the incident light. The applied voltage on Ag/AgCl scale has been converted to RHE scale using following expression:

$V_{RHE} = V_{Ag/AgCl} + 0.059\ pH + V^0_{Ag/AgCl}$

where $V^0_{Ag/AgCl} = 0.197$ V.

S3. IPCE calculation

The incident photon-to-current efficiency (IPCE) or external quantum efficiencies (EQEs) of the photoanodes was calculated under 420, 490 and 540 nm irradiation and applied voltage of +0.6 V *vs* Ag/AgCl (thermodynamic water splitting potential) using the following expression:

$$IPCE\ (\%) = \left[\frac{1240 \cdot J\ (mA\ cm^{-2})}{\lambda\ (\mathrm{nm}) \cdot \mathrm{P}\ (mW\ cm^{-2})}\right] 100$$

Where, *J* is the photocurrent density, λ is the wavelength of incident light and *P* is the incident light's power density.

S4. STH calculation

The solar-to hydrogen (STH) efficiency is calculated according to the following expression,

$$STH\ (\%) = \left[\frac{\Delta H.\Delta Gr}{Q.A.T}\right] 100$$

Where Q is the irradiation intensity, A is the irradiated area of the photoanode, and T is the irradiation time, while ΔH is the amount of hydrogen and ΔG_r is the Gibbs free energy change associated with the photocatalytic process.

S5. Faradaic efficiency calculation

Faradaic efficiency is defined as the ratio of observed H_2 under experimental condition divided by theoretically evolved H_2 calculated from photocurrent density according to the following expression.

$$Faradaic\ efficiency\ (\%) = \left[\frac{Experimental\ gas\ evolution\ (measured\ H_2)}{Theoretical\ H_2\ gas\ evolution\ (based\ on\ photocurrent)}\right] \cdot 100$$

$$Faradaic\ efficiency\ (\%) = \left[\frac{H_2\ evolution\ measured\ (mol)}{\frac{J\ (A\ cm^{-2}).A\ (cm^2).T\ (sec)}{2.e\ (C).N_A\ (mol^{-1})}}\right] \cdot 100$$

Where, J is the photocurrent density (A cm^{-2}), A is the irradiated area of the photoanode (cm^2), T is the PEC measurement time in seconds, e is the electron's charge (1.602 x 10^{-19} C) and N_A is the Avogadro number (6.02 x 10^{23} mol^{-1}).

S6. Note on effect of ion permeability of carbon nitride on the interpretation of Mott-Schottky data

Two phenomena occurring in carbon nitride thin films complicate the simplistic interpretation of the carrier densities extracted from Mott-Schottky (M-S) plots. The first is the injection of electrons from FTO:glass into the carbon nitride thin films and the capacitance step due to the injected charge is difficult to distinguish from the capacitance of the depletion layer intended to be measured via M-S plots.[1] The second problem is the well-known ion permeability of carbon nitride,[2-4] due to which ionic conduction disrupts the depletion layer capacitance through screening and other effects.[5] The net result is typically an overestimation of the carrier density. Therefore, the carrier density values listed in Table S6 ought to be treated with caution and interpreted qualitatively rather than quantitatively.

S7. Supporting Information Figures

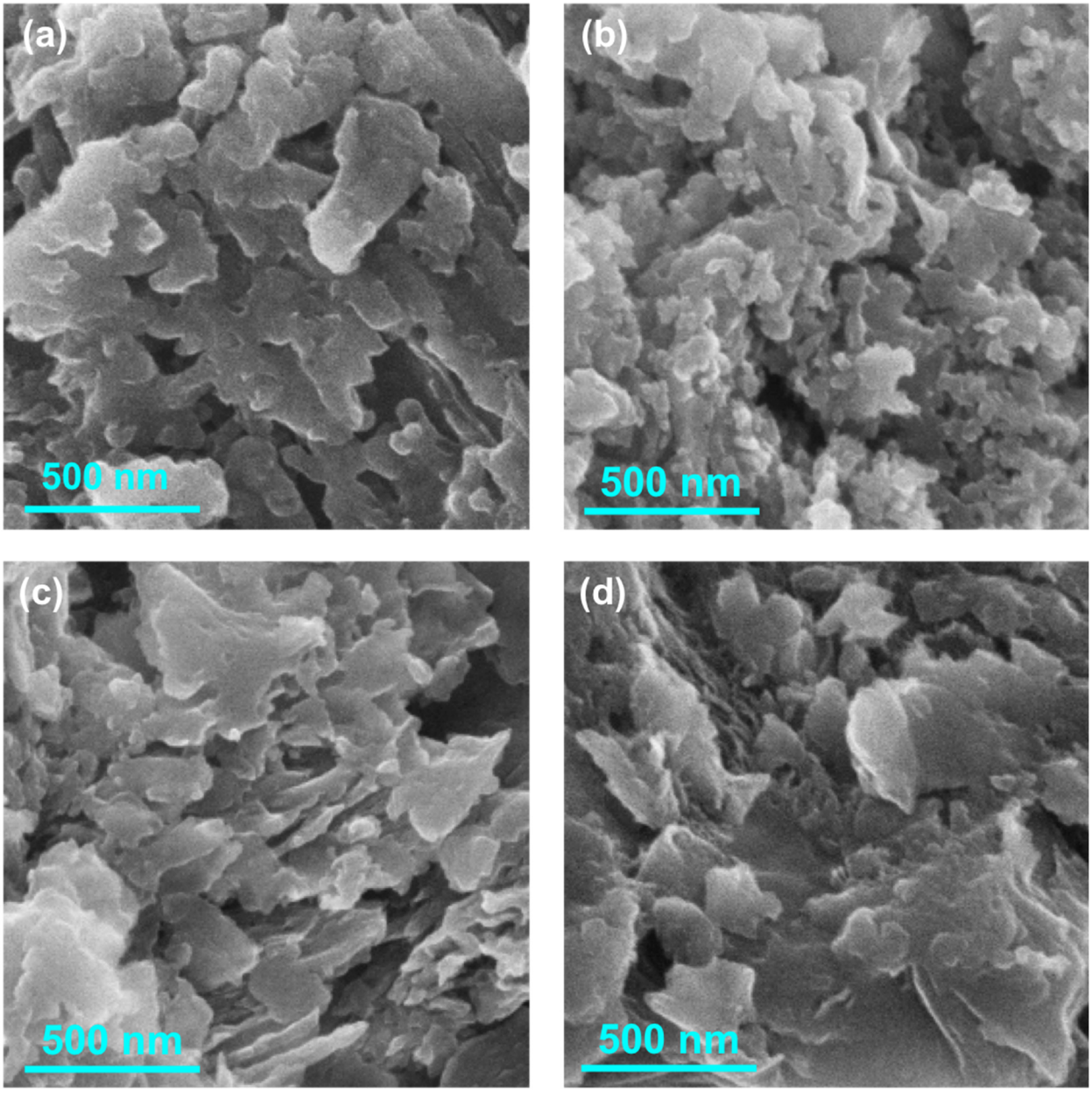

Figure S1. FESEM image of pure graphitic carbon nitride g-C_3N_4 (CN) (a) and *p*-PDA modified carbon nitrides (b) CN-C1 (c) CN-C3 and (d) CN-C6).

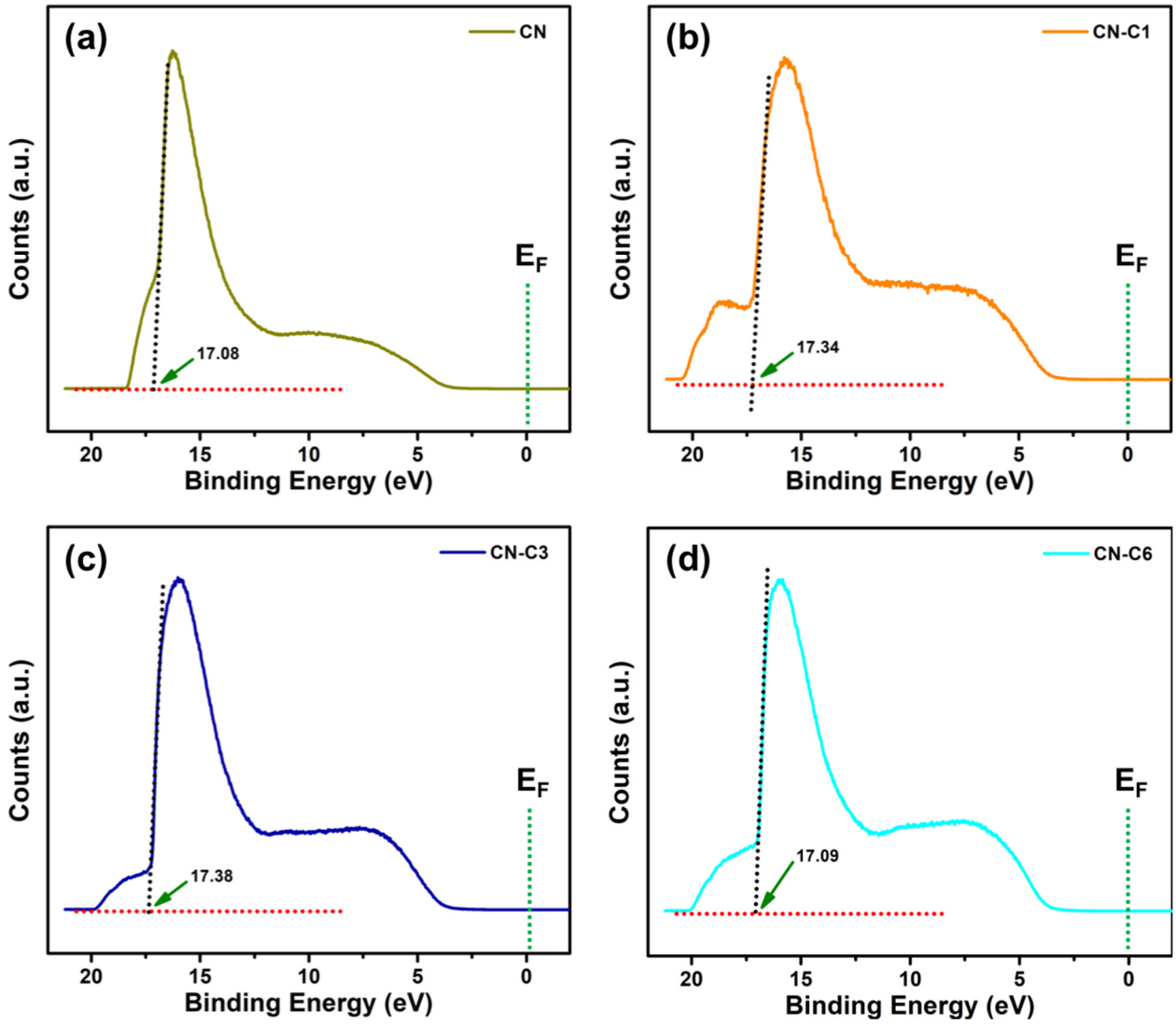

Figure S2. UPS work function (WF) spectra of (a) pure graphitic carbon nitride g-C_3N_4 (CN) and different *p*-PDA modified carbon nitrides (b) CN-C1, (c) CN-C3 and (d) CN-C6). The vertical dotted green line shows the position of Fermi level.

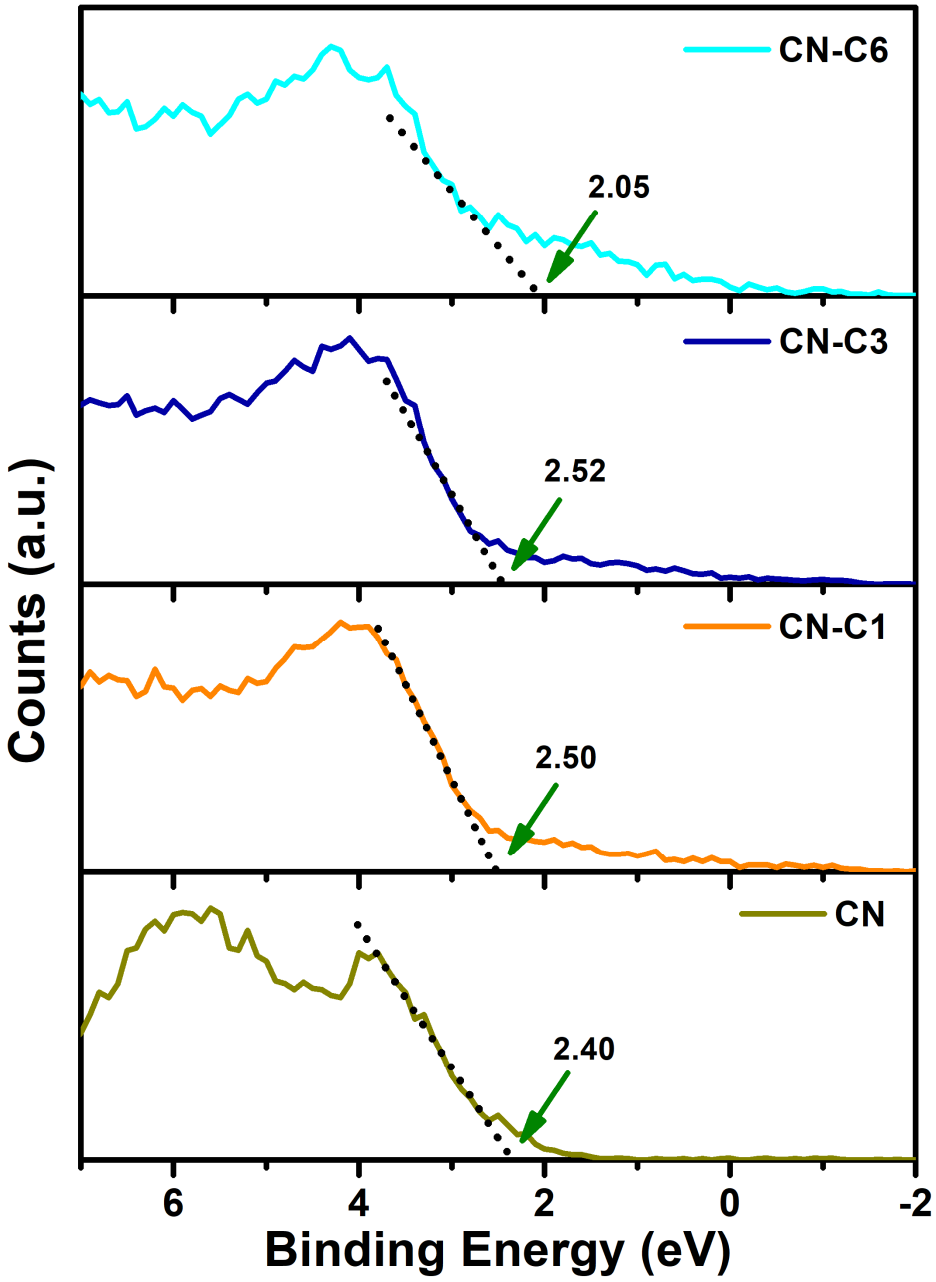

Figure S3. XPS valence band (VB) spectra of pure graphitic carbon nitride g-C_3N_4 (CN) and different *p*-PDA modified carbon nitrides (CN-C1, CN-C3 and CN-C6). The vertical dotted green line shows the position of Fermi level.

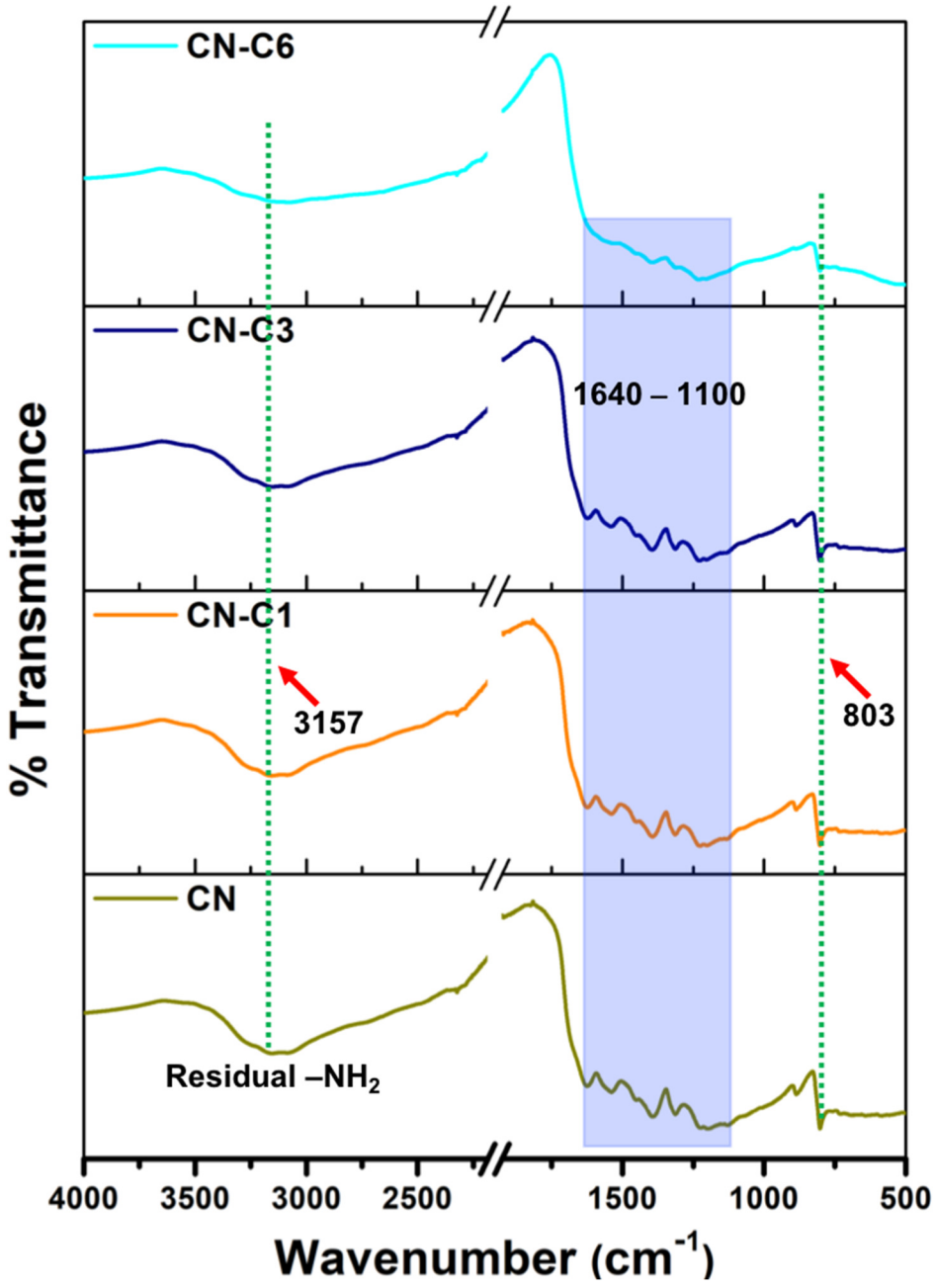

Figure S4. FTIR spectra of pure graphitic carbon nitride g-C_3N_4 (CN) and different *p*-PDA modified carbon nitrides (CN-C1, CN-C3 and CN-C6).

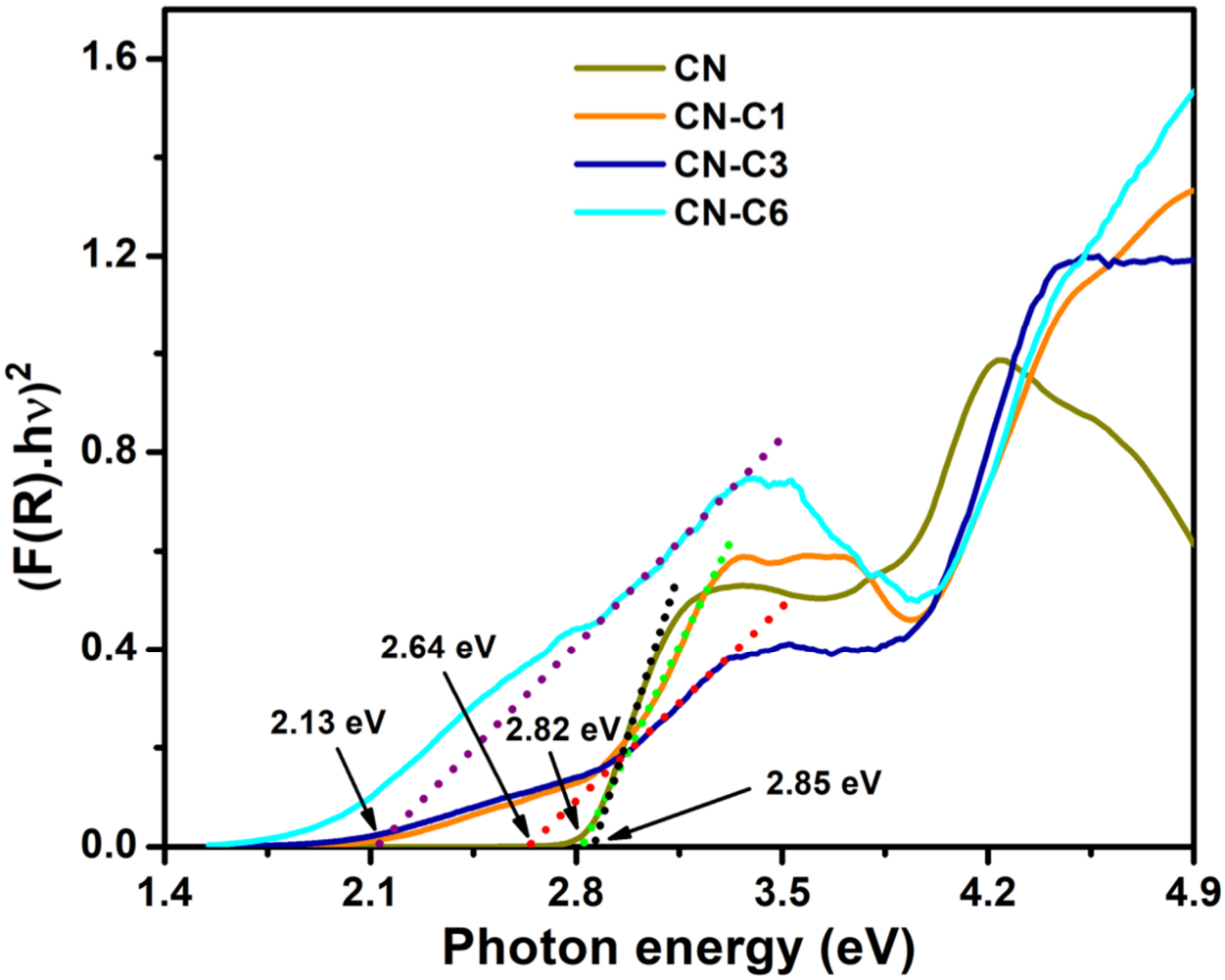

Figure S5. Kubelka-Munk function applied to DRS absorption data for the determination of the effective optical bandgaps of pure graphitic carbon nitride g-C_3N_4 (CN) and different *p*-PDA modified carbon nitrides (CN-C1, CN-C3 and CN-C6).

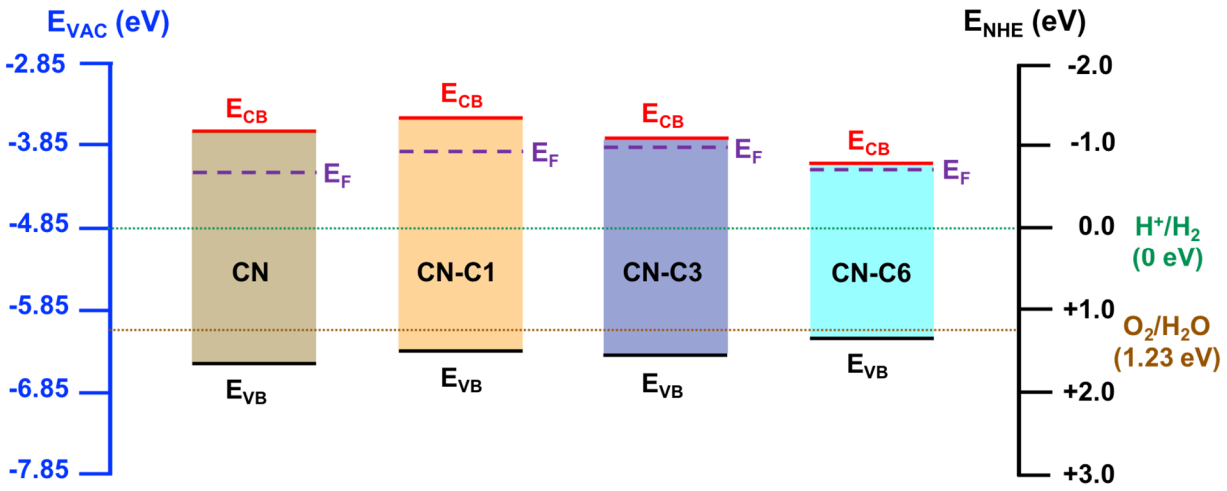

Figure S6. Position of Fermi level and electronic bands (conduction and valence bands) with respect to water-splitting redox potentials, obtained from UPS WF, XPS VB spectra and Kubelka-Munk function applied to DRS absorption spectra for pure graphitic carbon nitride g-C_3N_4 (CN) and different *p*-PDA modified carbon nitride hybrids (CN-C1, CN-C3 and CN-C6) in vacuum scale (left) and normal hydrogen electrode (NHE) scale (at pH 0) (right).

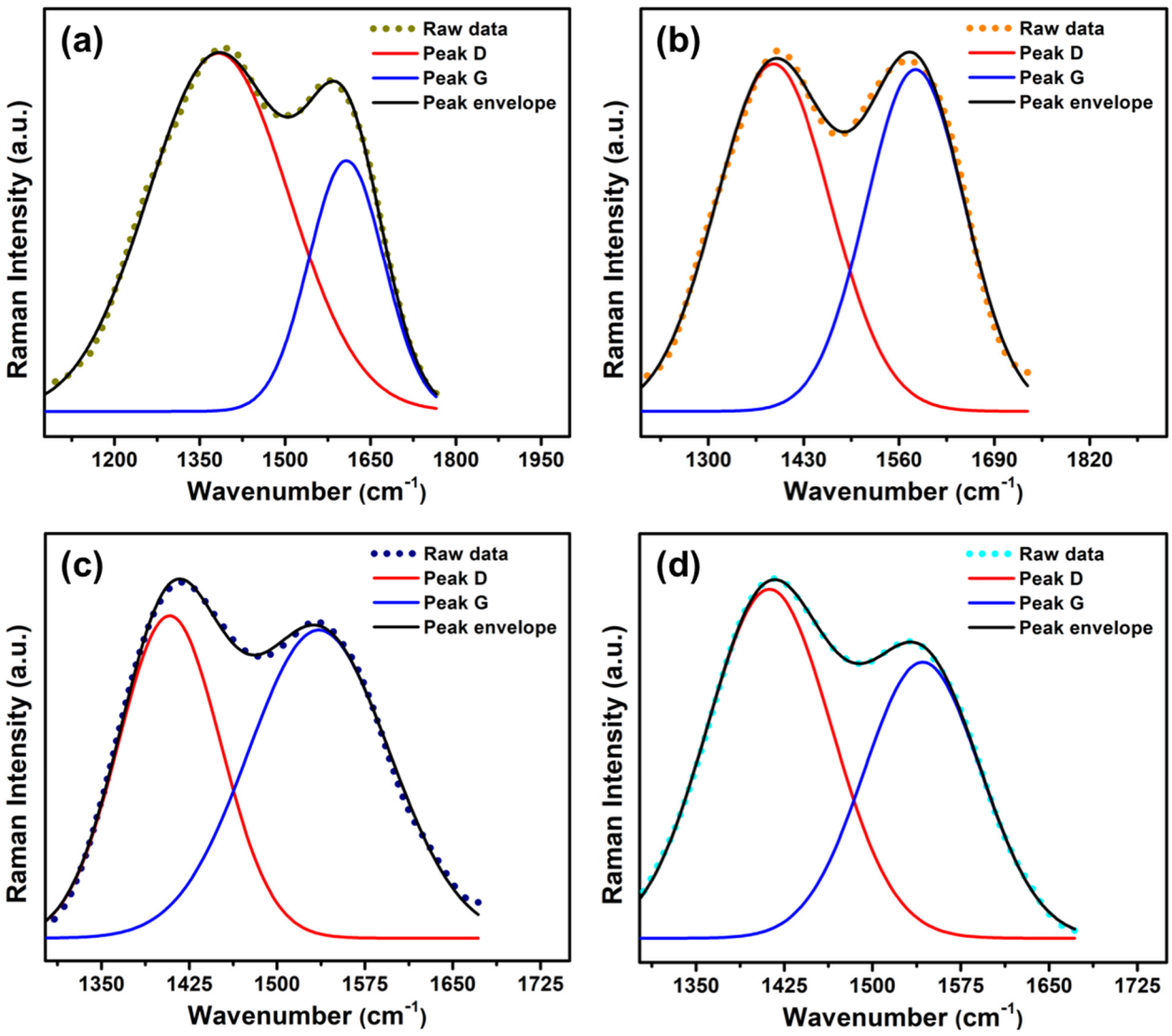

Figure S7. Deconvoluted Raman spectra (Figure 4b) showing the D and G bands of (a) pure graphitic carbon nitride g-C_3N_4 (CN) and different *p*-PDA modified carbon nitrides (b) CN-C1, (c) CN-C3 and (d) CN-C6).

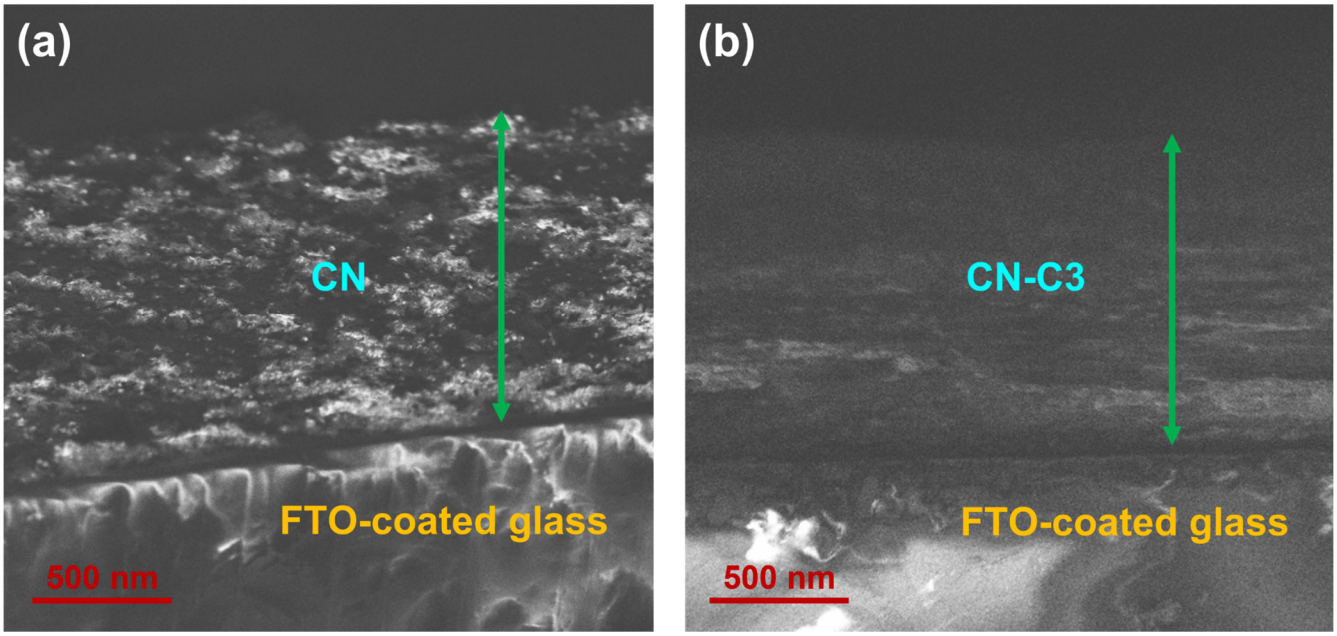

Figure S8. FESEM images of (a) pure graphitic carbon nitride g-C_3N_4 (CN) and (b) *p*-PDA modified carbon nitride CN-C3 films used for photoelectrochemical activity evaluation. The films' cross-sectional views show the film thickness (green arrow).

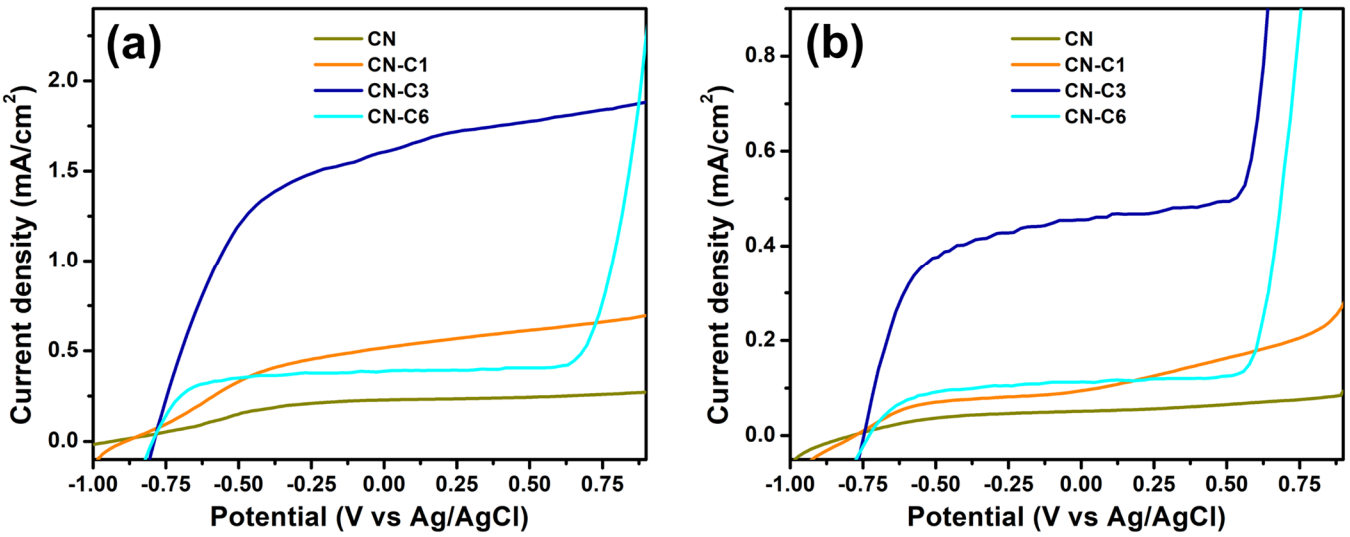

Figure S9. Photocurrent density *vs* applied bias at Ag vs Ag/AgCl scale under solar simulated AM1.5G light irradiation (100 mW cm^{-2}), (a) without and (b) with a 420 nm cut-off filter for pure graphitic carbon nitride g-C_3N_4 (CN) and *p*-PDA modified g-C_3N_4 (CN-C1, CN-C3 and CN-C6) samples.

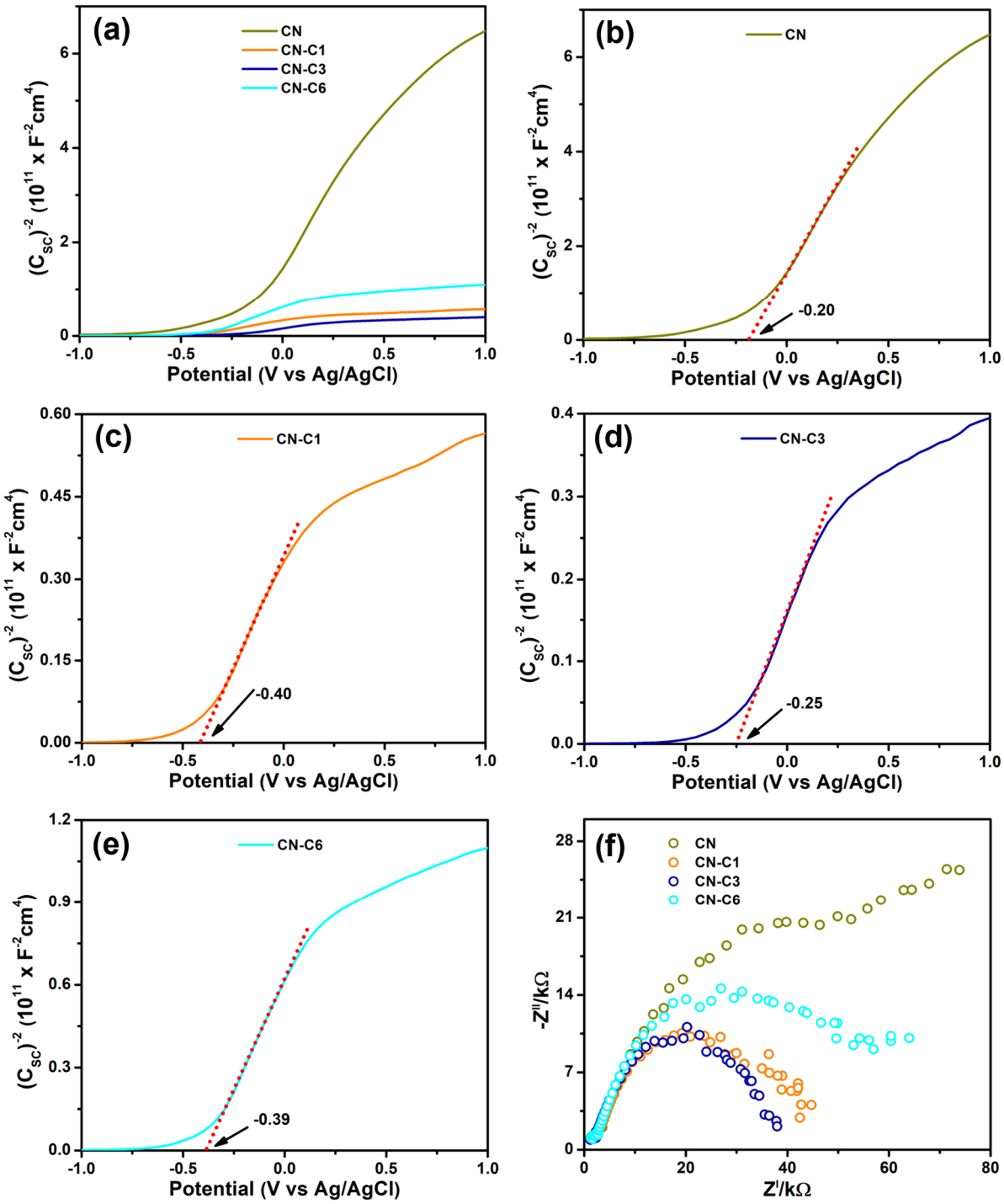

Figure S10. Mott-Schottky plots of (a) pure graphitic carbon nitride g-C_3N_4 (CN) and (b)-(e) *p*-PDA modified g-C_3N_4 (CN-C1, CN-C3 and CN-C6) samples. (f) Nyquist plots obtained from electrochemical impedance spectroscopy (EIS) of pure graphitic carbon nitride g-C_3N_4 (CN) and *p*-PDA modified g-C_3N_4 (CN-C1, CN-C3 and CN-C6) samples.

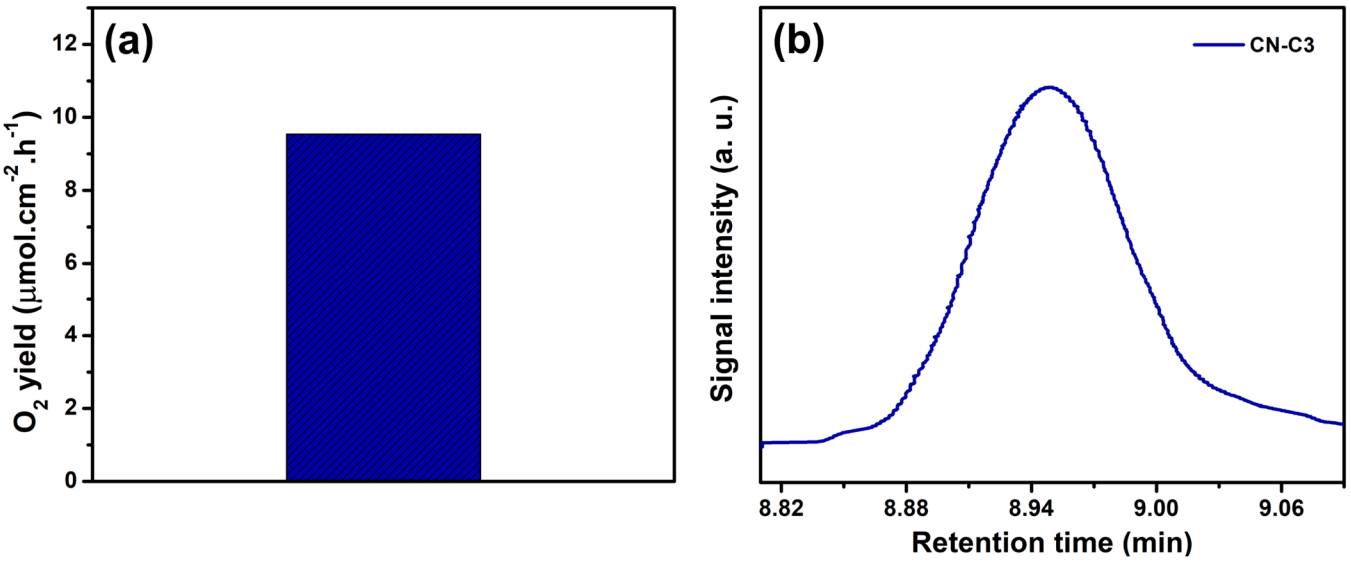

Figure S11. (a) Oxygen evolution rate per unit illumination area for CN-C3 sample. (b) GC chromatogram of collected oxygen at photoanode in photoelectrochemical water splitting experiment for CN-C3 sample.

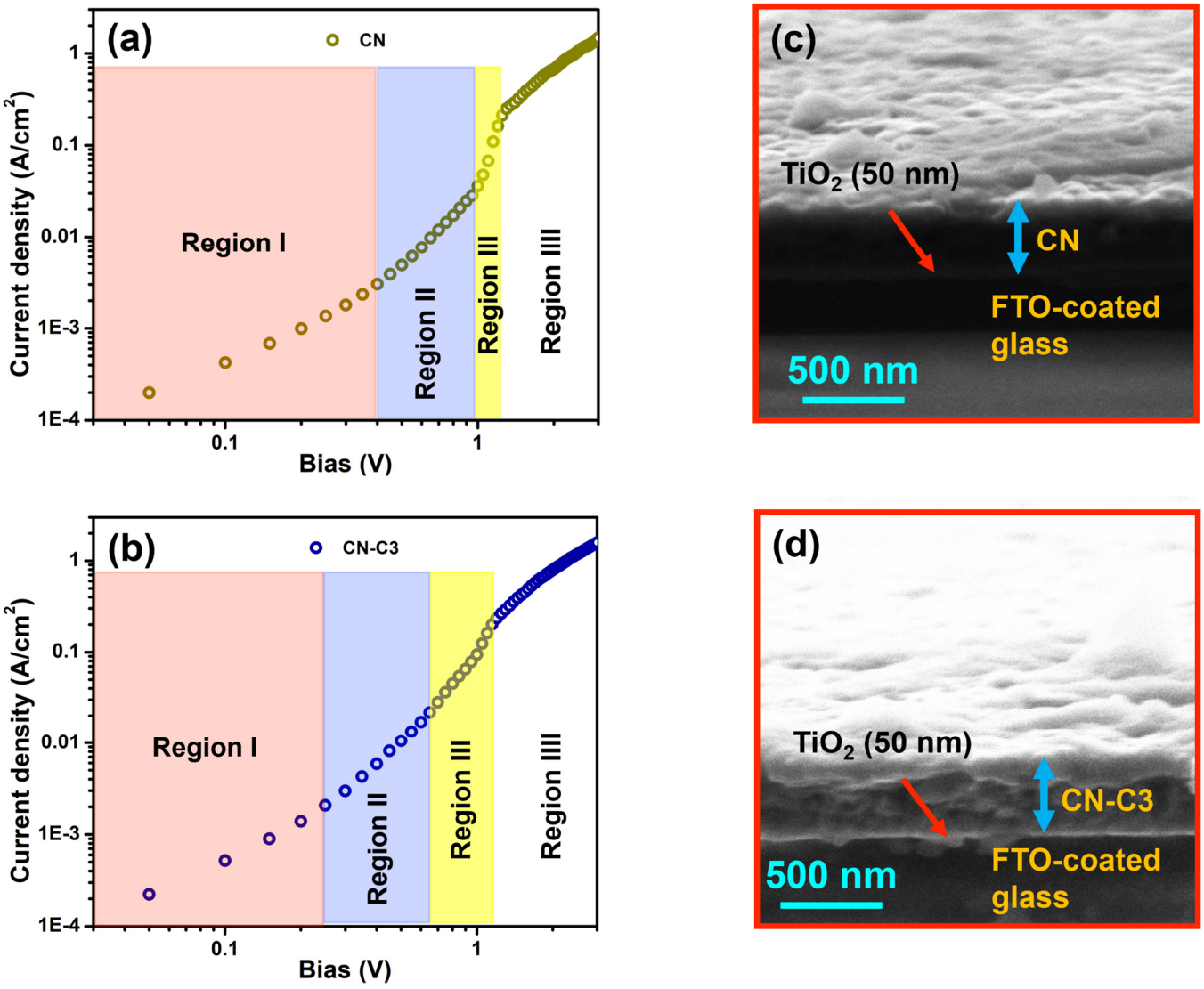

Figure S12. Log–log plot of the steady state current density–voltage (*J*-*V*) characteristics of (a) pure graphitic carbon nitride g-C_3N_4 (CN) and (b) *p*-PDA modified carbon nitride CN-C3. Different transport regimes for both samples are identified and marked; FESEM images showing the cross-sectional views for the determination of film thickness for (c) pure graphitic carbon nitride g-C_3N_4 (CN) and (d) *p*-PDA modified carbon nitride CN-C3.

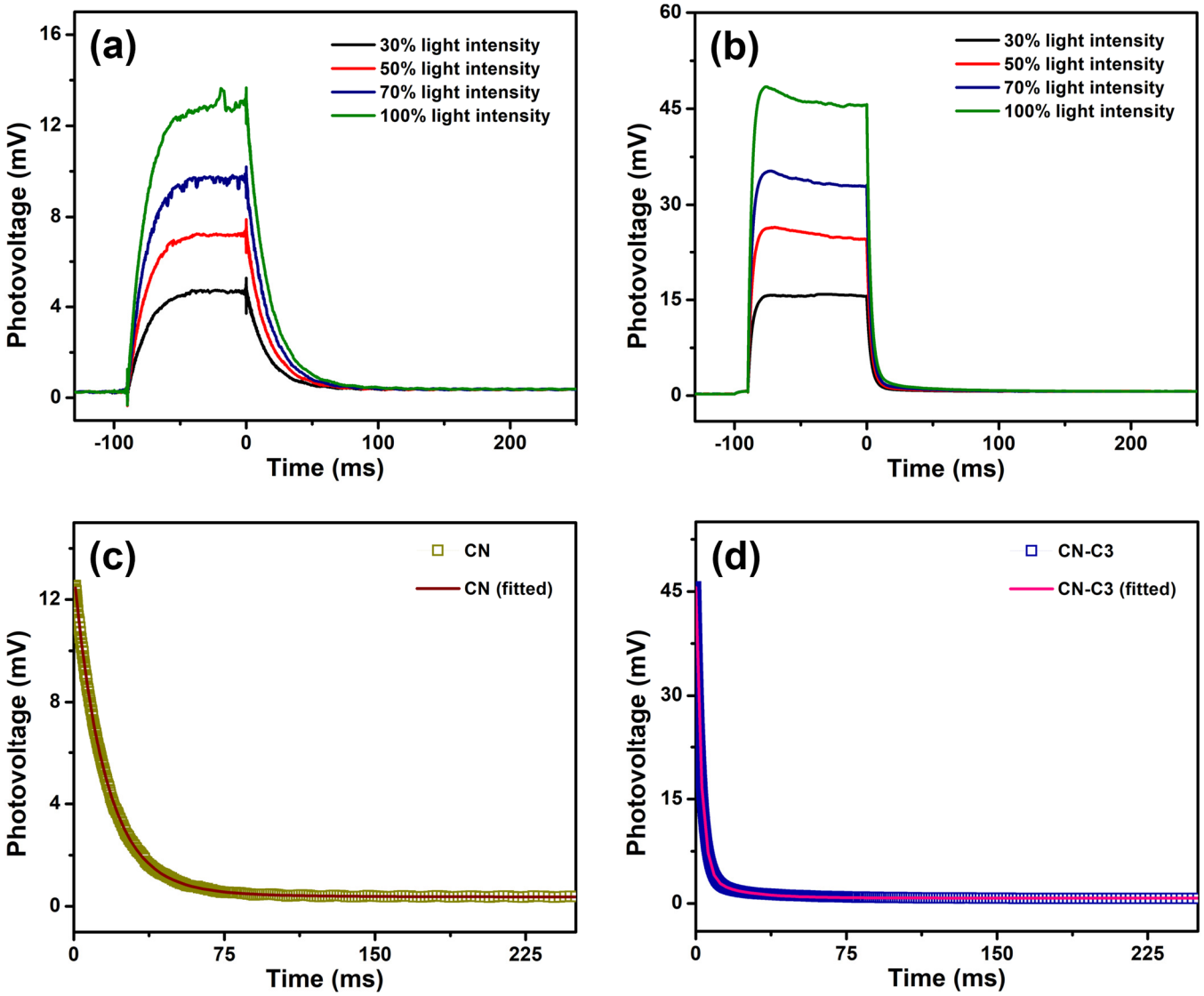

Figure S13. Photovoltage (PV) and transient photovoltage (TPV) plots at variable light intensities for (a) pure graphitic carbon nitride g-C_3N_4 (CN) and (b) *p*-PDA modified carbon nitride CN-C3; Biexponential fitting of TPV transients obtained at 100% light intensity for (c) pure graphitic carbon nitride g-C_3N_4 (CN) and (d) *p*-PDA modified carbon nitride CN-C3.

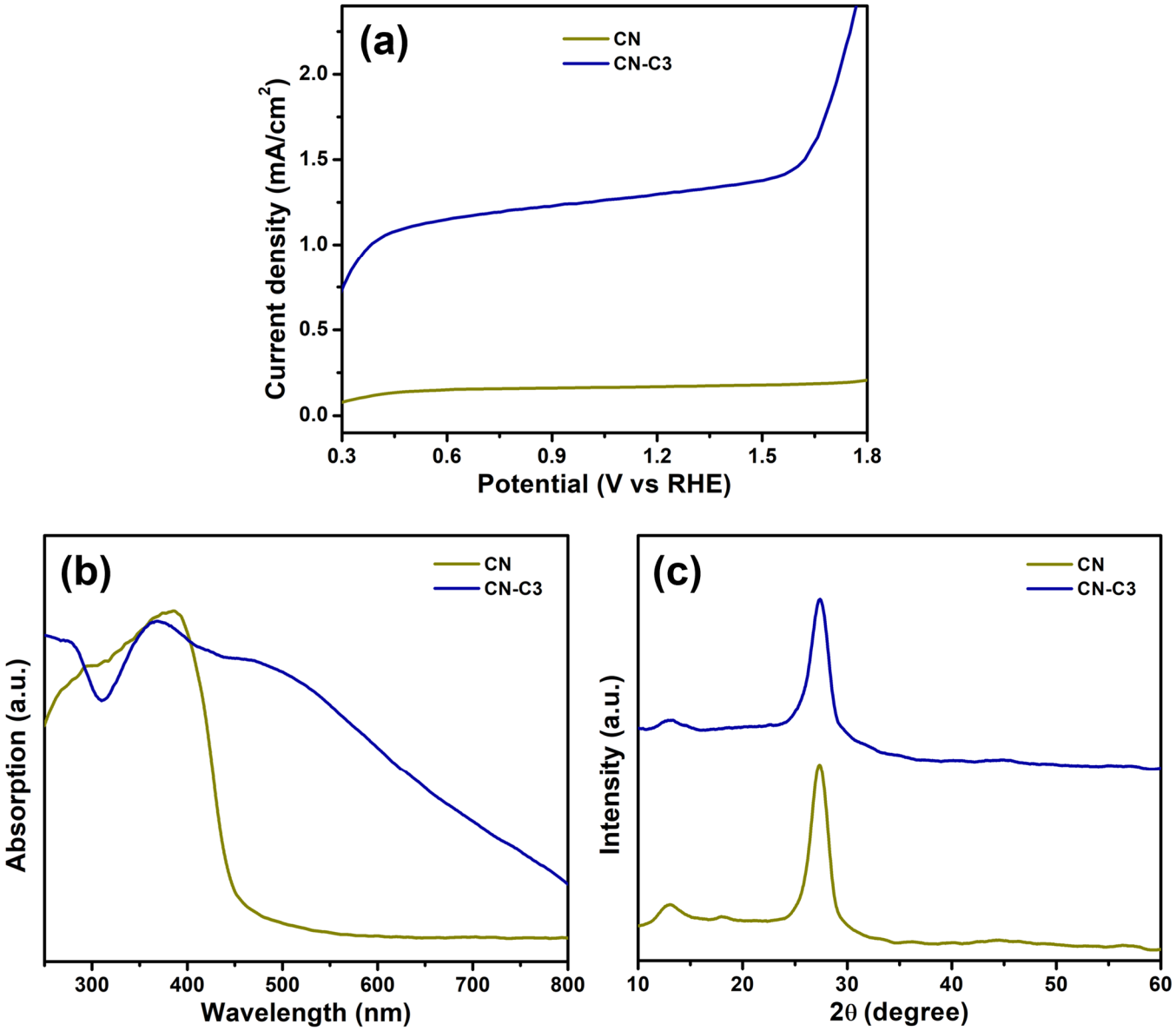

Figure S14. (a) Photocurrent *vs* applied bias at RHE (reversible hydrogen electrode)under solar simulated AM1.5G light irradiation (100 mW cm^{-2}) without a 420 nm cut-off filter for previously used pure graphitic carbon nitride g-C_3N_4 (CN) and *p*-PDA modified g-C_3N_4 (CN-C3) samples. Characterization data of post-stability samples for g-C_3N_4 (CN) and *p*-PDA modified g-C_3N_4 (CN-C3); (b) Diffuse reflectance absorption spectra (DRS) and (c) X-ray diffractograms (XRD).

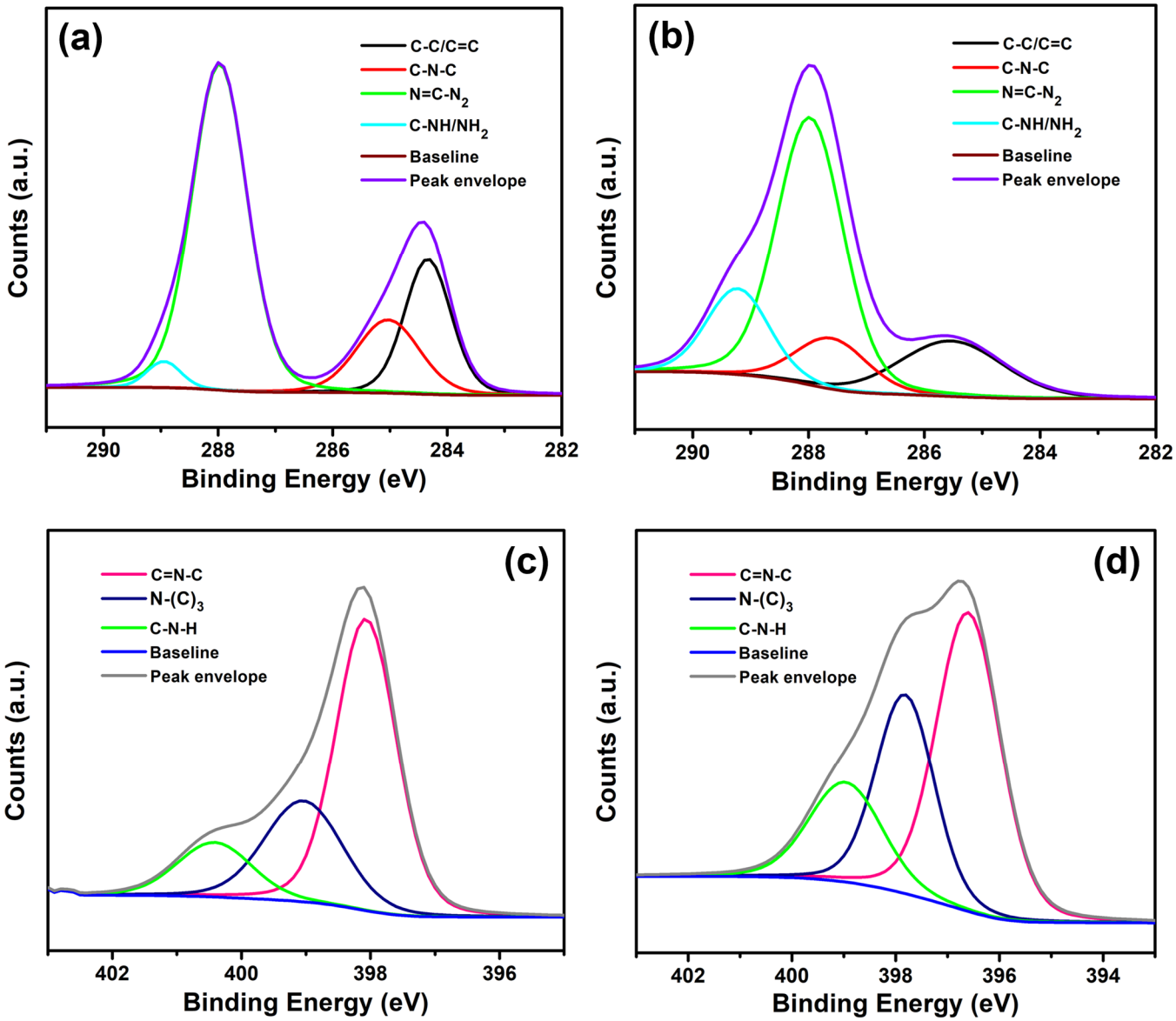

Figure S15. Core-level HRXPS spectra of post-stability samples in C1s region for (a) g-C_3N_4 (CN) and (b) *p*-PDA modified g-C_3N_4 (CN-C3) samples; in N1s region for (a) CN and (b) CN-C3.

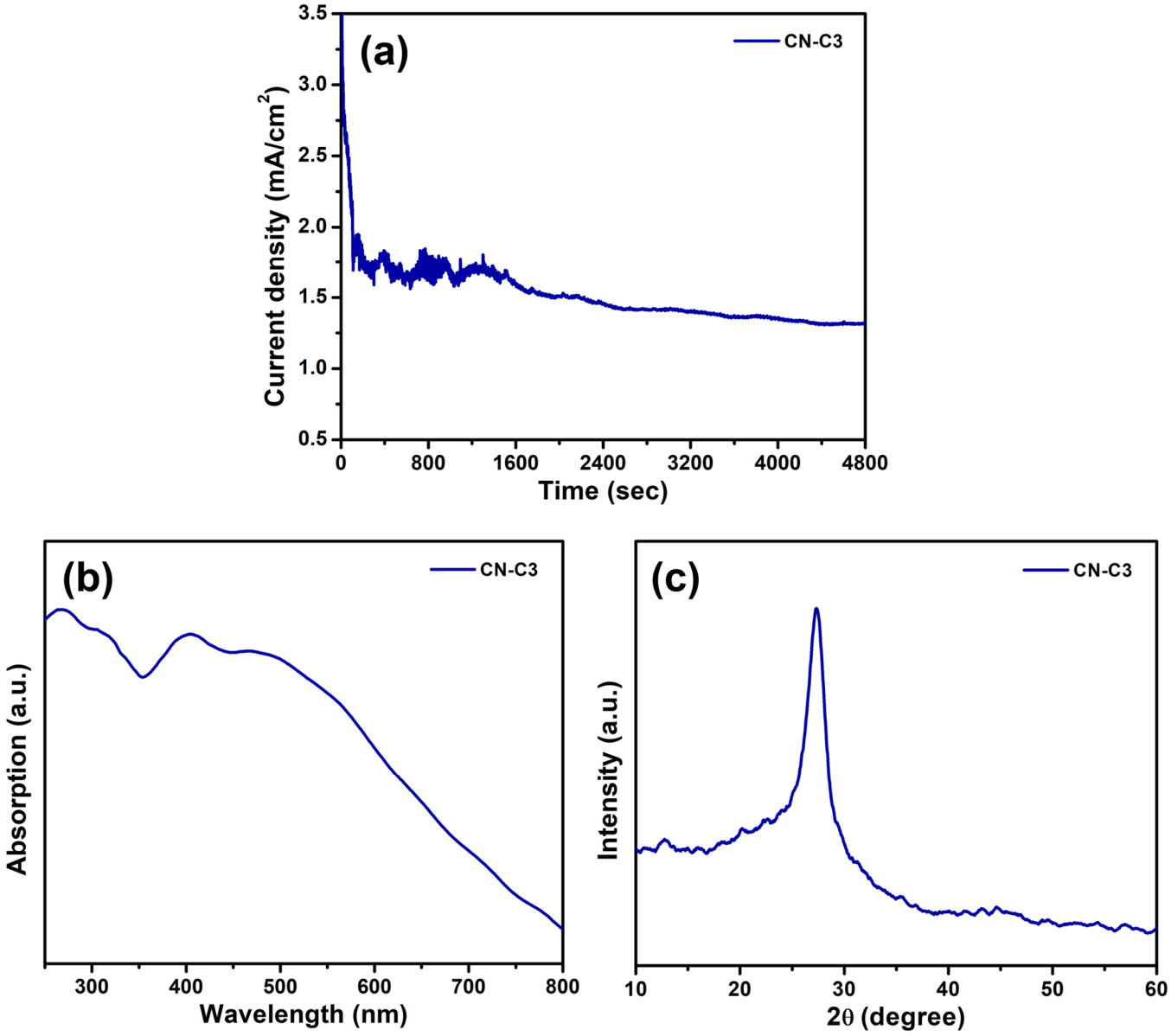

Figure S16. (a) Photocurrent *vs* time at 1.623 V bias (RHE scale) under solar simulated AM1.5G light irradiation (100 mW cm^{-2}) without a 420 nm cut-off filter for *p*-PDA modified g-C_3N_4 (CN-C3) sample. Characterization data of post-stability samples for *p*-PDA modified g-C_3N_4 (CN-C3) sample; (b) Diffuse reflectance absorption spectra (DRS) and (c) X-ray diffractograms (XRD).

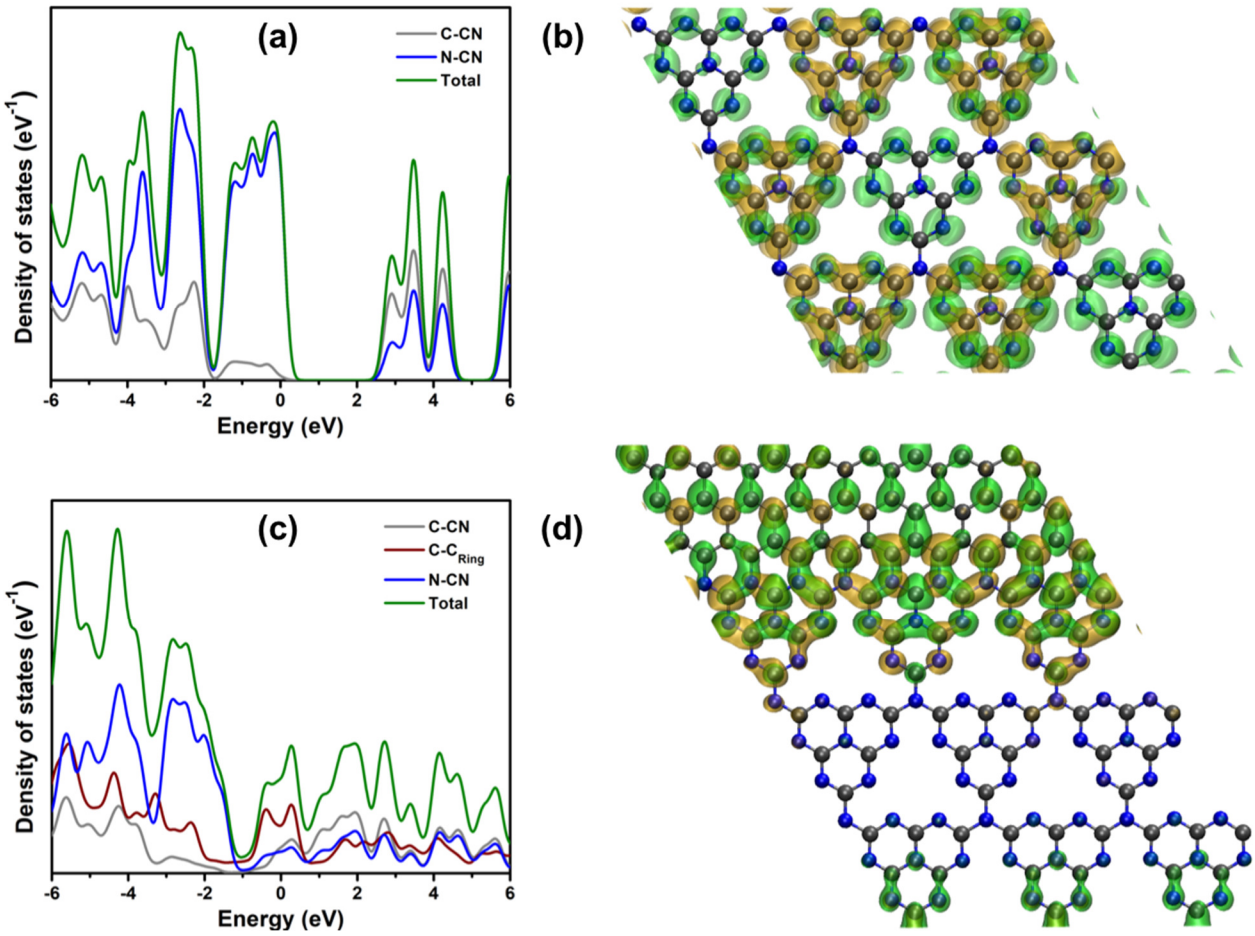

Figure S17. Partial density of states obtained by summing up the projected density of states (PDOS) of selected atoms from the DFT optimized systems of (a) single layer tri-s-triazine (heptazine) based g-C_3N_4 and (c) single layer g-C_3N_4 conjugated to C-ring units. Spatial distributions of molecular orbitals of DFT optimized systems of (b) single layer tri-s-triazine (heptazine) based g-C_3N_4 and (d) single layer g-C_3N_4 conjugated to C-ring units. The transparent green and orange surfaces represent highest occupied molecular orbital (HOMO) and lowest unoccupied molecular orbital (LUMO) respectively. Grey and blue colours are for C and N atoms respectively.

S7. Supporting Information Tables

Table S1. CHN combustion data showing relative amount of C, N and H for different samples.

Element/ Sample	CN	CN-C1	CN-C2	CN-C3	CN-C4	CN-C5	CN-C6
C	35.11	35.20	35.44	36.29	36.94	37.43	42.98
N	62.28	61.09	60.41	58.74	58.39	57.65	51.03
H	1.81	1.80	1.79	1.78	1.82	1.81	1.84

Table S2. FESEM-EDX data showing relative amount of C and N for different samples.

Element/ Sample	CN	CN-C1	CN-C3	CN-C6
C	38.42	39.91	42.23	50.58
N	61.58	60.09	57.77	49.42

Table S3. Peak area ratio (A_G/A_D), FWHM of D and G bands of different samples shown in Figure 4(b) & Figure S7.

Sample	Peak area ratio (A_G/A_D)	FWHM (Peak D)	FWHM (Peak G)
CN	0.38	290.63	155.41
CN-C1	0.85	182.99	157.82
CN-C3	1.32	102.57	141.20
CN-C6	0.74	123.97	116.47

Table S4. Calculated average lifetimes of different samples from time-resolved photoluminescence (TRPL) spectra shown in Figure 4(d).

Sample	Decay time (ns)			Relative amplitude (%)			Average lifetime (ns)
	τ_1	τ_2	τ_3	A_1	A_2	A_3	τ_{avg}
CN	1.01	3.44	17.44	58.3	35.8	5.9	7.99
CN-C1	1.61	0.41	5.50	44.7	43.2	12.1	3.14
CN-C3	0.50	1.69	5.65	52.0	39.9	8.1	2.77
CN-C6	1.94	0.52	5.90	47.7	39.2	13.1	3.40

Table S5. BET surface area and pore dimension of different samples shown in Figure 4(f).

Sample	Surface area (m^2/g)	Pore volume (cc/g)	Pore diameter (nm)
CN	5.801	0.063	3.054
CN-C1	13.591	0.202	3.053
CN-C3	11.880	0.166	3.053
CN-C6	13.907	0.341	6.506

Table S6. Calculated carrier concentrations and flat band potentials of different samples from Mott-Schottky spectra shown in Figure S10.

Sample	Carrier concentration (cm^{-3})	Flat band potential (V vs Ag/AgCl)
CN	3.03E+19	-0.20
CN-C1	2.84E+20	-0.40
CN-C3	3.79E+20	-0.25
CN-C6	1.42E+20	-0.39

Table S7. Calculated average lifetimes of different samples from transient photovoltage (TPV) spectra shown in Figure S12.

Sample	Decay time (ms)		Relative amplitude (%)		Average lifetime (ms)
	τ_1	τ_2	A_1	A_2	τ_{avg}
CN	15.08	38.74	93.3	6.7	18.77
CN-C3	18.59	2.66	7.75	92.25	8.55

References

(1) Ravishankar, S.; Bisquert, J.; Kirchartz, T. Interpretation of Mott–Schottky plots of photoanodes for water splitting. *Chemical Science* **2022**, *13* (17), 4828–4837, 10.1039/D1SC06401K. DOI: 10.1039/D1SC06401K.
(2) Wang, Y.; Wu, N.; Wang, Y.; Ma, H.; Zhang, J.; Xu, L.; Albolkany, M. K.; Liu, B. Graphite phase carbon nitride based membrane for selective permeation. *Nature Communications* **2019**, *10* (1), 2500. DOI: 10.1038/s41467-019-10381-z.
(3) Liu, Z.; Jiang, X.; Chen, J.; Liu, W.; Zhao, L.; Lv, Y.; Li, Z.; Zhang, Y.; Wang, X.; Zhang, S. Ionogel electrolyte based on porous graphitic C3N4 nanosheets for room temperature to 150 °C quasi-solid-state lithium batteries. *Journal of Energy Chemistry* **2025**, *104*, 494–504. DOI: https://doi.org/10.1016/j.jechem.2025.01.032.
(4) Ye, M.; Li, B.; Zhang, K.; Yan, R.; Dai, L.; Zhang, S.; Li, Y.; Hu, J.; Yang, B.; Yao, Y. Application of graphitic carbon nitride (g-C3N4) in solid polymer electrolytes: A mini review. *Electrochemistry Communications* **2025**, *176*, 107939. DOI: https://doi.org/10.1016/j.elecom.2025.107939.
(5) Lin, F.; Bachman, B. F.; Boettcher, S. W. Impact of Electrocatalyst Activity and Ion Permeability on Water-Splitting Photoanodes. *The Journal of Physical Chemistry Letters* **2015**, *6* (13), 2427–2433. DOI: 10.1021/acs.jpclett.5b00904.